

In vivo demonstration of reflection artifact reduction in photoacoustic imaging using synthetic aperture photoacoustic-guided focused ultrasound (PAFUSion)

MITHUN KUNIYIL AJITH SINGH,^{1,*} MICHAEL JAEGER,² MARTIN FRENZ,²
AND WIENDEL STENBERGEN¹

¹Biomedical Photonic Imaging Group, MIRA institute for Biomedical Technology and Technical Medicine, University of Twente, P.O. Box 217, 7500 AE Enschede, The Netherlands

²Institute of Applied Physics, University of Bern, Sidlerstrasse 5, 3012 Bern, Switzerland
[*m.kuniylajithsingh@utwente.nl](mailto:m.kuniylajithsingh@utwente.nl)

Abstract: Reflection artifacts caused by acoustic inhomogeneities are a critical problem in epi-mode biomedical photoacoustic imaging. High light fluence beneath the probe results in photoacoustic transients, which propagate into the tissue and reflect back from echogenic structures. These reflection artifacts cause problems in image interpretation and significantly impact the contrast and imaging depth. We recently proposed a method called PAFUSion (Photoacoustic-guided focused ultrasound) to identify such reflection artifacts in photoacoustic imaging. In its initial version, PAFUSion mimics the inward-travelling wavefield from small blood vessel-like PA sources by applying ultrasound pulses focused towards these sources, and thus provides a way to identify the resulting reflection artifacts. In this work, we demonstrate reduction of reflection artifacts in phantoms and *in vivo* measurements on human volunteers. In view of the spatially distributed PA sources that are found in clinical applications, we implemented an improved version of PAFUSion where photoacoustic signals are backpropagated to imitate the inward travelling wavefield and thus the reflection artifacts. The backpropagation is performed in a synthetic way based on the pulse-echo acquisitions after transmission on each single element of the transducer array. The results provide a direct confirmation that reflection artifacts are prominent in clinical epi-photoacoustic imaging, and that PAFUSion can strongly reduce these artifacts to improve deep-tissue photoacoustic imaging.

©2016 Optical Society of America

OCIS codes: (170.5120) Photoacoustic imaging; (170.7170) Ultrasound; (170.3880) Medical and biological imaging.

References and links

1. P. Beard, "Biomedical photoacoustic imaging," *Interface Focus* **1**(4), 602–631 (2011).
2. M. Xu and L. V. Wang, "Photoacoustic imaging in biomedicine," *Rev. Sci. Instrum.* **77**, 041101 (2006).
3. S. Hu and L. V. Wang, "Photoacoustic imaging and characterization of the microvasculature," *J. Biomed. Opt.* **15**(1), 011101 (2010).
4. H. F. Zhang, K. Maslov, G. Stoica, and L. V. Wang, "Functional photoacoustic microscopy for high-resolution and noninvasive *in vivo* imaging," *Nat. Biotechnol.* **24**(7), 848–851 (2006).
5. X. L. Dean-Ben and D. Razansky, "Adding fifth dimension to optoacoustic imaging: volumetric time-resolved spectrally enriched tomography," *Light Sci. Appl.* **3**, e137 (2014).
6. X. L. Deán-Ben, E. Bay, and D. Razansky, "Functional optoacoustic imaging of moving objects using microsecond-delay acquisition of multispectral three-dimensional tomographic data," *Sci. Rep.* **4**, 5878 (2014).
7. A. Hussain, W. Petersen, J. Staley, E. Hondebrink, and W. Steenbergen, "Quantitative blood oxygen saturation imaging using combined photoacoustics and acousto-optics," *Opt. Lett.* **41**(8), 1720–1723 (2016).
8. S. A. Ermilov, T. Khamapirad, A. Conjusteau, M. H. Leonard, R. Lacewell, K. Mehta, T. Miller, and A. A. Oraevsky, "Laser optoacoustic imaging system for detection of breast cancer," *J. Biomed. Opt.* **14**(2), 024007 (2009).
9. M. Heijblom, D. Piras, M. Brinkhuis, J. C. G. van Hespren, F. M. van den Engh, M. van der Schaaf, J. M. Klaase, T. G. van Leeuwen, W. Steenbergen, and S. Manohar, "Photoacoustic image patterns of breast carcinoma and comparisons with Magnetic Resonance Imaging and vascular stained histopathology," *Sci. Rep.* **5**, 11778 (2015).
10. P. van Es, S. K. Biswas, H. J. Bernelot Moens, W. Steenbergen, and S. Manohar, "Initial results of finger imaging using photoacoustic computed tomography," *J. Biomed. Opt.* **19**(6), 060501 (2014).

11. X. Wang, J. Jo, G. Xu, A. Marquardt, S. Francis, G. Gandikota, and J. Yuan, "Photoacoustic imaging of human inflammatory arthritis," in proceedings of IEEE International Ultrasonics Symposium (IUS, 2015), pp. 1–4.
12. L. Xi and H. B. Jiang, "High resolution three-dimensional photoacoustic imaging of human finger joints in vivo," *Appl. Phys. Lett.* **107**, 063701 (2015).
13. D. R. Bauer, R. Olafsson, L. G. Montilla, and R. S. Witte, "3-D photoacoustic and pulse echo imaging of prostate tumor progression in the mouse window chamber," *J. Biomed. Opt.* **16**(2), 026012 (2011).
14. C. L. Bayer, Y. S. Chen, S. Kim, S. Mallidi, K. Sokolov, and S. Emelianov, "Multiplex photoacoustic molecular imaging using targeted silica-coated gold nanorods," *Biomed. Opt. Express* **2**(7), 1828–1835 (2011).
15. M. Kuniyil Ajith Singh, W. Steenbergen, and S. Manohar, "Handheld Probe-Based Dual Mode Ultrasound/Photoacoustics for Biomedical Imaging," in *Frontiers in Biophotonics for Translational Medicine*, M. Olivo and U. S. Dinis, eds. (Springer Singapore, 2016), pp. 209–247.
16. J. J. Niederhauser, M. Jaeger, R. Lemor, P. Weber, and M. Frenz, "Combined ultrasound and optoacoustic system for real-time high-contrast vascular imaging in vivo," *IEEE Trans. Med. Imaging* **24**(4), 436–440 (2005).
17. R. G. M. Kolkman, P. J. Brands, W. Steenbergen, and T. G. van Leeuwen, "Real-time in vivo photoacoustic and ultrasound imaging," *J. Biomed. Opt.* **13**(5), 050510 (2008).
18. A. Aguirre, P. Guo, J. Gamelin, S. Yan, M. M. Sanders, M. Brewer, and Q. Zhu, "Coregistered three-dimensional ultrasound and photoacoustic imaging system for ovarian tissue characterization," *J. Biomed. Opt.* **14**(5), 054014 (2009).
19. M. Jaeger, L. Siegenthaler, M. Kitz, and M. Frenz, "Reduction of background in optoacoustic image sequences obtained under tissue deformation," *J. Biomed. Opt.* **14**(5), 054011 (2009).
20. K. Daoudi, P. J. van den Berg, O. Rabot, A. Kohl, S. Tisserand, P. Brands, and W. Steenbergen, "Handheld probe integrating laser diode and ultrasound transducer array for ultrasound/photoacoustic dual modality imaging," *Opt. Express* **22**(21), 26365–26374 (2014).
21. C. Kim, T. N. Erpelding, L. Jankovic, M. D. Pashley, and L. V. Wang, "Deeply penetrating in vivo photoacoustic imaging using a clinical ultrasound array system," *Biomed. Opt. Express* **1**(1), 278–284 (2010).
22. G. Xu, J. R. Rajian, G. Girish, M. J. Kaplan, J. B. Fowlkes, P. L. Carson, and X. Wang, "Photoacoustic and ultrasound dual-modality imaging of human peripheral joints," *J. Biomed. Opt.* **18**(1), 010502 (2012).
23. A. Needles, A. Heinmiller, J. Sun, C. Theodoropoulos, D. Bates, D. Hirson, M. Yin, and F. S. Foster, "Development and Initial Application of a Fully Integrated Photoacoustic Micro-Ultrasound System," *IEEE Trans. Ultrason. Ferroelectr. Freq. Control* **60**(5), 888–897 (2013).
24. M. Jaeger, J. C. Bamber, and M. Frenz, "Clutter elimination for deep clinical optoacoustic imaging using localised vibration tagging (LOVIT)," *Photoacoustics* **1**(2), 19–29 (2013).
25. M. Kuniyil Ajith Singh and W. Steenbergen, "Photoacoustic-guided focused ultrasound (PAFUSion) for identifying reflection artifacts in photoacoustic imaging," *Photoacoustics* **3**(4), 123–131 (2015).
26. M. Jaeger, D. Harris-Birtill, A. Gertsch, E. O'Flynn, and J. Bamber, "Deformation-compensated averaging for clutter reduction in epiphotoacoustic imaging *in vivo*," *J. Biomed. Opt.* **17**(6), 066007 (2012).
27. G. Held, S. Preisser, H. G. Akarçay, S. Peeters, M. Frenz, and M. Jaeger, "Effect of irradiation distance on image contrast in epi-optoacoustic imaging of human volunteers," *Biomed. Opt. Express* **5**(11), 3765–3780 (2014).
28. E. J. Alles, M. Jaeger, and J. C. Bamber, "Photoacoustic Clutter Reduction Using Short-Lag Spatial Coherence Weighted Imaging," in proceedings of IEEE International Ultrasonics Symposium (IUS, 2014), pp. 41–44.
29. H. M. Schwab, M. F. Beckmann, and G. Schmitz, "Photoacoustic clutter reduction by inversion of a linear scatter model using plane wave ultrasound measurements," *Biomed. Opt. Express* **7**(4), 1468–1478 (2016).
30. X. L. Deán-Ben, V. Ntziachristos, and D. Razansky, "Artefact reduction in optoacoustic tomographic imaging by estimating the distribution of acoustic scatterers," *J. Biomed. Opt.* **17**(11), 110504 (2012).
31. T. F. Fehm, X. L. Deán-Ben, and D. Razansky, "Four dimensional hybrid ultrasound and optoacoustic imaging via passive element optical excitation in a hand-held probe," *Appl. Phys. Lett.* **105**(17), 173505 (2014).
32. M. Jaeger, S. Schupbach, A. Gertsch, M. Kitz, and M. Frenz, "Fourier reconstruction in optoacoustic imaging using truncated regularized inverse k-space interpolation," *Inverse Probl.* **23**(6), S51–S63 (2007).
33. D. Piras, C. Grijsen, P. Schütte, W. Steenbergen, and S. Manohar, "Photoacoustic needle: minimally invasive guidance to biopsy," *J. Biomed. Opt.* **18**(7), 070502 (2013).
34. W. Xia, D. I. Nikitichev, J. M. Mari, S. J. West, R. Pratt, A. L. David, S. Ourselin, P. C. Beard, and A. E. Desjardins, "Performance characteristics of an interventional multispectral photoacoustic imaging system for guiding minimally invasive procedures," *J. Biomed. Opt.* **20**(8), 086005 (2015).
35. M. A. Lediju Bell, N. P. Kuo, D. Y. Song, J. U. Kang, and E. M. Boctor, "In vivo visualization of prostate brachytherapy seeds with photoacoustic imaging," *J. Biomed. Opt.* **19**(12), 126011 (2014).

1. Introduction

Photoacoustic (PA) imaging, also called optoacoustic imaging, is an emerging medical imaging modality. PA imaging is performed using short-pulsed visible or near-infrared light, which, while absorbed by molecules such as hemoglobin in blood, generates ultrasound (US) due to the thermoelastic effect. The US is measured at the surface of tissue using US detectors, and the location and spatial details of the absorber are reconstructed from the acquired US signals [1, 2]. PA imaging offers excellent optical contrast combined with ultrasonic resolution for structural and functional medical imaging. Since different light-absorbing chromophores in tissue (hemoglobin, lipids, fat etc) have their own characteristic

absorption spectrum, it is possible to distinguish these using spectroscopic PA imaging [1]. PA imaging holds promise in functional imaging of the vasculature [3], in particular for differentiating oxygen levels based on the different optical absorption characteristics of oxy and deoxy-hemoglobin [4–7]. This technique has potential to diagnose vascular diseases, inflammations and cancer at an early stage [8–12], and for monitoring the disease response to specific medications/treatments [13]. In addition to the tissue chromophores, external contrast agents functionalized for specific biochemical targets hold potential in early detection of diseases [14].

Of the different medical imaging modalities, pulse-echo US imaging is largely prevalent, considering the compactness, affordability and real-time performance for point-of-care applications. Since the detection part is the same for pulse-echo US and PA imaging, PA imaging can be easily realized in a US scanner just by adding a light delivery system and a trigger control to a commercial US-system [15]. The impact and importance of dual-mode PA/US systems for improving clinical diagnostics has been demonstrated [16–23]. Handheld dual-mode US/PA probes use reflection-mode imaging geometry (epi-mode), where optical components are directly integrated into [20] or attached to the US probe such that the light illumination is done from the same side where PA signals are detected. Bearing in mind the clinical scenario, this can help the doctors to use free-hand guidance of the probe with maximum fluence below the probe for optimal SNR. Importantly, bony and acoustically attenuating soft tissue (large breast, abdomen, limbs) can be imaged only in epi-mode as these structures obstruct propagation of acoustic waves from the irradiated tissue region to the acoustic probe [24].

Epi-illumination has however a downside; high light fluence beneath and proximal to the probe generates PA transients from superficial optical absorbers (i.e. melanin or blood vessels), which propagate into the tissue and reflect back from echogenic structures to produce reflection artifacts (echo clutter) [19, 24, 25]. These reflection artifacts severely limit the contrast and imaging depth [24, 26, 27]. In addition, when imaging structures which are acoustically inhomogeneous and optically absorbing, reflection artifacts may appear in the region of interest and be misinterpreted as real optically absorbing structures [25]. Also, the high intensity reflection artifacts overshadow the weak PA signals from deep tissue structures where fluence is less. These artifacts cannot be reduced by signal averaging. It has been shown in human volunteers that reflection artifacts can be minimized by irradiating the skin surface outside the imaging plane in a dark-field approach [27]. However, the benefit of such an approach is limited, and it comes at the cost of a low SNR. It is therefore not feasible with integrated systems [20] that provide pulse energies in the few mJ range, because they require illuminating the tissue directly below the probe to achieve a suitable SNR. For these reasons, clinically successful high-contrast PA imaging requires methods for reducing reflection artifacts.

Several methods have been studied for identifying and reducing reflection artifacts in PA imaging [24, 26, 28, 29]. LOVIT [24] and DCA [26] aim at reducing reflection artifacts that occur below a certain depth (typically below 15 mm). Because they require a local tissue displacement relative to the skin surface, they are not suited for reducing artifacts close to the skin. This is especially a disadvantage with low-energy integrated systems that are designed for a shallow imaging depth, but where the in-plane irradiation results in strong reflections of the PA transient generated in the skin melanin layer. Reflections are also considered to be significant in PA tomography of small animals, and techniques for artifact reduction have been proposed for implementation in hybrid PA and US tomography systems [30, 31].

We recently reported on the proof-of-principle of a novel method called PAFUSion [25]. In its initial version, PAFUSion mimics the inward-travelling wavefield from small blood vessel-like PA sources by applying US pulses focused towards these sources, and thus provides a way to identify reflection artifacts. PAFUSion specifically targets at in-plane reflection artifacts, which are prominent when tissue is irradiated in-line with the US imaging plane. In this work, we demonstrate reflection-artifact-correction in addition to identification, towards obtaining an artifact-free PA image in quasi-real-time. In view of clinical applications

where realistic PA sources can include a number of blood vessels of various sizes and extended structures such as the skin melanin layer, we implemented an improved version of PAFUSion that is more versatile than the previous focusing approach. We propose to employ synthetic backpropagation of PA signals for mimicking the inward-travelling PA field and thus the reflection artifacts caused by a complex distribution of PA sources. Backpropagation is based on reference pulse-echo US data that are obtained with element-by-element transmission. By subtracting the synthetically generated artifact signal from the detected PA signal, reflection artifacts can be significantly reduced. Because PAFUSion is equally suited for reducing superficial as well as deep reflection artifacts, it solves the limitation of previously reported approaches.

The goal of this paper is to present our first results of reflection artifact correction in PA images using improved PAFUSion. We demonstrate strong in-plane artifact reduction in phantom and *in vivo* measurements on forearm of human volunteers. Uncorrected epi-mode PA images and PAFUSion-corrected PA images are thoroughly compared to demonstrate the impact and importance of our method in biomedical photoacoustics.

2. Theory

PAFUSion is based on the concept that the PA wavefield can be decomposed into two parts P_o and P_i that propagate into opposite directional half-spaces. If the total wavefield is considered as a superposition of plane-wave components, part P_o comprises all plane-waves with wave vectors pointing into the half-space towards the skin surface. At the time $t = 0$, immediately after irradiating a hypothetical Dirac delta laser pulse but before transients start propagating, the local vibrational velocity is zero. In line with a general concept in PA imaging, each plane-wave in P_o has therefore a counterpart with equal amplitude and wave number but opposite propagation direction. The superposition of all these counterparts constitutes the wavefield P_i . From the initial condition of zero vibrational velocity, it therefore follows that the two wavefields can be written as time-inverted aliases:

$$P_i(\mathbf{r}, t) = P_o(\mathbf{r}, -t), \quad (1)$$

where r denotes the spatial coordinates inside the tissue.

Figure 1(a) illustrates the fields P_o and P_i that propagate towards the probe and into the tissue, respectively, for the case where skin absorption is the main source of reflection artifacts. Both P_o and P_i are scattered by echogenic structures inside the tissue and may produce reflection artifacts. However, it is assumed that (i) mainly the part propagating into the tissue leads to significant reflection artifacts. Assumption (i) is motivated by the exponential attenuation of the irradiating laser light in epi-PA imaging, together with the rather weak US scattering of tissue: Reflection artifacts that are comparable in amplitude to the weak PA signals from inside the tissue stem from reflections of the stronger PA transients generated closer to the skin surface. Figure 1(a) illustrates the signal time traces recorded by an US array probe. They contain the directly detected PA signals from the skin and from deeper blood vessels as well as the echoes caused by back-reflection of the inward-propagating skin PA transient. Further assumptions include:

- (ii) There exists a time T that fulfills following two conditions: All PA sources that are strong enough to produce significant echoes lead to a direct signal that is detected within the time interval $[0, T]$, and the earliest detected echoes arrive at $t > T$. A possible selection of T is indicated in Fig. 1(a).
- (iii) The aperture and the spatial sampling (element pitch) of the transducer array are sufficient to detect the full wavefield P_o .
- (iv) The array elements have an isotropic Dirac delta receive and transmit impulse response, and acoustic attenuation is negligible.

If assumptions (i) to (iv) are fulfilled, re-transmission of the PA signal that was detected within the time interval $[0, T]$ leads to the reproduction of the echoes that were contained in

the PA signal. Subtraction of these echoes from the original PA data results in reflection-artifact reduction. This principle is explained in more detail in the following.

The detected echoes can be modelled as the result of a linear operator H acting onto the wavefield P_i . H describes the influence of the spatial distribution of mechanical properties in a linear system theory approach, as a linear transformation from arbitrary wavefields (a function of spatial coordinate \mathbf{r} and time t) to the detected echo signals (as a function of array element index n and time t). For simplicity of notation, the operation of H is written as a convolution. According to assumption (iv) the signal S detected on elements n is equal to the wavefield sampled at the element positions \mathbf{r}_n , and with the help of assumption (i) and the definition of H , S can be written as:

$$S(n, t) = P_o(\mathbf{r}_n, t) + H(\mathbf{r}, t \rightarrow n, t) * P_i(\mathbf{r}, t). \quad (2)$$

According to assumptions (iii) and (iv), excitation of the transducer elements with the signal S after time-inversion leads to physical back-propagation of a time-inverted alias of the detected wavefield. According to assumption (ii), S is identical to P_o on the time interval $[0, T]$. Therefore, re-transmission of the signal detected during the time interval $[0, T]$ results in a time-inverted alias P_o' of the echo-producing part of P_o :

$$P_o'(\mathbf{r}, t') = P_o(\mathbf{r}, T - t'). \quad (3)$$

Figure 1(b) illustrates the physical backpropagation for the skin absorption signal. The signal that was detected during $[0, T]$ is time-inverted and re-transmitted into the tissue. At time $t' = T$, the wavefield P_o' converges to the origin of the original PA transient. For $t' > T$ the backpropagating wavefield replicates the original inward-travelling wavefield P_i . Defining $t^* = t' - T$:

$$P_i^*(\mathbf{r}, t^*) \equiv P_o'(\mathbf{r}, t^* + T) = P_o(\mathbf{r}, T - t^* - T) = P_o(\mathbf{r}, -t^*) = P_i(\mathbf{r}, t^*). \quad (4)$$

P_i^* is reflected in the same way as P_i , resulting in the detection of a signal S^* that contains the same echoes as the ones that were present in the original PA signal at $t > T$ (see Fig. 1(c) for illustration). Subtraction of S^* from the original S will therefore yield an echo-free PA signal. For brevity, variables \mathbf{r} , n and t will be omitted in H :

$$S^*(n, t^*) = H * P_i^*(\mathbf{r}, t^*) = H * P_i(\mathbf{r}, t = t^*), \quad (5)$$

$$S(n, t) - S^*(n, t^* = t) = P_o(\mathbf{r}_n, t) + H * [P_i(\mathbf{r}, t) - P_i^*(\mathbf{r}, t^* = t)] = P_o(\mathbf{r}_n, t). \quad (6)$$

Whereas an isotropic Dirac delta impulse response was assumed so far (assumption iv), typical clinical probes have a limited bandwidth and angle-dependent transmit and receive characteristics. This is not a strong limitation to the technique, because differences in the transducer impulse responses for PA detection and US transmission/detection can be compensated for by filtering operations. To allow detection and backpropagation of arbitrary wavefields according to assumptions (iii) and (iv), a probe would require an infinite 2D aperture and an omnidirectional receive and transmit response. In reality, the limited probe aperture and the finite element pitch, together with a limited directional response, do not allow detecting and imitating arbitrary wavefields. For that reason, backpropagation is only applicable within further constraints to P_o and thus to the geometry of optical absorbers. In the case of blood vessels or point-like absorbers, the laterally propagating part of the transients cannot be detected and thus reflection artifacts generated by these transients cannot be mimicked via backpropagation. In a similar way as for assumption (i), one may argue that the most significant echoes will be produced by the axially propagating part of the transients. When using a linear probe, only transients propagating parallel to the imaging plane can be mimicked. Such transients are generated by cylindrical or flat tissue structures (such as e.g. blood vessels, the skin melanin layer) when they are oriented perpendicular to the imaging plane.

Taking into account these experimental limitations, the less general statement of Eq. (6) is that echoes can be reduced within the systems frequency bandwidth, and depending on proper alignment of the probe relative to the reflection artifact-generating tissue structures.

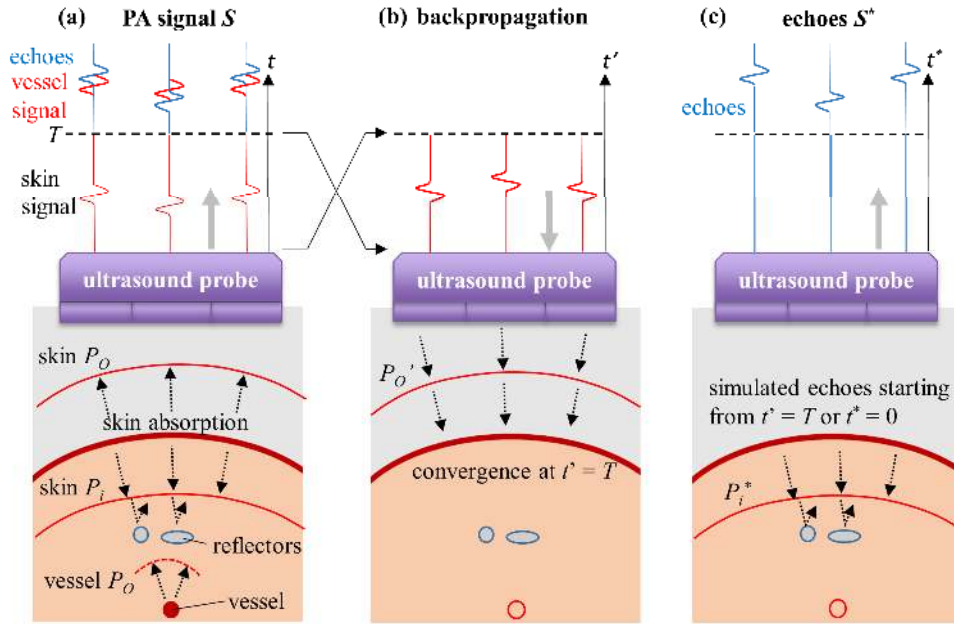


Fig. 1. (a) Illustration of inward (P_i) and outward-propagating (P_o) PA transients, for the special case where they are generated by optical absorption in the skin melanin layer. (b) Time-inversion and backpropagation of the PA signal from interval $t = [0, T]$, towards (c) mimicking the inward-travelling wavefield P_i^* and identification of resulting echoes.

2.1 Synthetic PA backpropagation based on reference pulse-echo data

To avoid motion artifacts, physical backpropagation requires immediate re-transmission of detected PA signals. To be able to do so, an ideal PAFUSion system would require the front-end hardware facilities for recording PA signals, performing the filter operations for transducer impulse response matching, and re-transmitting arbitrary waveforms. In a typical state-of-the-art system, however, these facilities will not be available. Instead of a physical backpropagation, we therefore propose a synthetic approach. This approach is based on post-processing pulse-echo acquisitions that are obtained after transmitting on single elements at a time. These data can be acquired in immediate succession with PA data with a minimum time delay. The concept of synthetic PA backpropagation using element-wise pulse-echo acquisitions is based on writing the backpropagated wavefield P_i^* as a superposition of the wavefields $P_{i,n}^*$ produced by back-propagation from single elements n . The wavefield produced by each single element can in turn be written as a convolution of the time-inverted PA signal S detected on that element, with the wavefield $P_{\delta,n}$ produced by transmission of a Dirac delta pulse on that element:

$$P_i^*(\mathbf{r}, t^*) = \sum_n P_{i,n}^*(\mathbf{r}, t^* = t^* + T) = \sum_n \int_0^T dt' S(n, T - t') \cdot P_{\delta,n}(\mathbf{r}, t^* - t'). \quad (7)$$

Correspondingly, the echoes S^* detected upon backpropagation of P_i^* can be written as a superposition of the echoes S_n^* detected on elements n^* after backpropagation of the wavefields $P_{i,n}^*$ from elements n . This in turn can be written as a convolution of the echoes $S_{\delta,n}$ detected after transmitting Dirac delta pulses on elements n , convolved with the time-inverted signal from the respective same element:

$$\begin{aligned}
 S^*(n^*, t^*) &= \sum_n S_n^*(n^*, t'' = t^* + T) = \sum_n \int_0^T dt' S(n, T - t') \cdot [H^* P_{\delta, n}](n^*, t'' - t') \\
 &\equiv \sum_n \int_0^T dt' S(n, T - t') \cdot S_{\delta, n}(n^*, t'' - t').
 \end{aligned}
 \tag{8}$$

Therefore, backpropagation can be performed in a synthetic way using the following algorithm:

- Record pulse-echo signals $S_{\delta, n}(n^*, t')$ on elements n^* after transmission of Dirac delta pulses on each element n
- Time-invert the PA signals $S(n, t)$ detected during the interval $t = [0, T]$
- Numerically convolve the time inverted signals with the signals $S_{\delta, n}(n^*, t')$, shift in time according to $t^* = t'' - T$
- Superimpose the results to form $S^*(n^*, t^*)$

The reference pulse-echo data acquired for synthetic backpropagation can be a collection of acquisitions on all elements n^* , after transmissions on elements n as described so far. Alternatively, synthetic backpropagation can be based on any other collection of US data that provides sufficient information, such as a collection of plane-wave acquisitions with different transmit steering angles.

3. Materials and methods

3.1 Equipment and setup

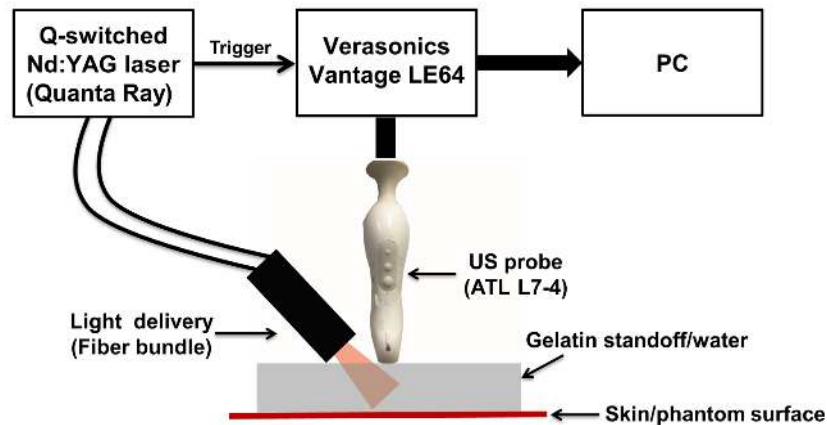


Fig. 2. Illustration of the experimental setup.

For the phantom and *in vivo* studies, an epi-mode combined PA and US system was used as shown in Fig. 2. Image acquisition was implemented on a Vantage 64 LE data acquisition system (VDAS, Verasonics Inc., Redmond, WA), which can read data from 64 channels at a time, and perform continuous data transfer for real-time processing on a host PC via a pci-e interface (6.6 GByte/s sustained transfer rate). The processing and the order in which different software scripts are executed are explained in section 3.2. The US probe used for the experiment was a linear array transducer (ATL L7-4, Philips N.V., NL), containing 128 elements at a pitch of 0.3 mm with a center frequency of 5 MHz and fractional bandwidth of 80%. For avoiding reflection artifacts caused by optical absorption in the rubber material of the transducer aperture, the aperture was optically shielded with a thin aluminum foil acoustically coupled with US gel. A Q-switched Nd:YAG laser (Quanta Ray, Newport, CA) provided pulsed laser light at a wavelength of 1064 nm with a pulse duration of 10 ns and a

repetition rate of 10 Hz. The output of the laser was coupled into an 8 mm diameter optical fiber bundle (Fiberoptics, Switzerland), with a rectangular distal fiber terminal (20 mm x 1 mm) aligned parallel to the linear transducer array.

In all experiments, the output angle of the fiber terminal was aligned in such a way that the location of main optical absorption coincided with the transducer's imaging plane. On one hand, this irradiation geometry resulted in high fluence below the US probe and thus optimum PA signal-to-noise ratio. On the other hand, it was required to make sure that reflection artifacts were generated only by PA transients that could be simulated by US transmission. The area of illumination on the skin was 3 mm by 23 mm, resulting in a radiant exposure of 70 mJ/cm² which was well below the limit of the maximum permissible exposure (MPE) for skin (100 mJ/cm² at 1064 nm).

3.2 Experimental implementation of the synthetic backpropagation technique

A scan sequence script for defining the acquisition of PA and US data by the VDAS as well as post-processing routines for synthetic backpropagation and image display on the host PC were programmed in Matlab. The Verasonics sequence executor (VSX) software executed the scan sequence and post-processing.

In a first step, the scan sequence defined the acquisition of pulse-echo data on all elements per transmission on each single element. To minimize acquisition time and thus the influence of tissue motion, all data were buffered on the VDAS' local memory before transferring to a first buffer frame on the host PC. In a second step, PA data were acquired and transferred to a second buffer frame. As a third step, for creating memory for storing the PAFUSion data to be obtained later (see below), a dummy PA acquisition was defined in the scan sequence, without a preceding laser pulse but with all other specifications identical to the real PA acquisition. An external function performed the synthetic backpropagation of the PA data (second frame) according to the convolution approach in Eq. (8), based on the element-wise pulse-echo data (first frame). When acquiring the pulse-echo data, care was taken to use a low transmit voltage and to make sure that the signal amplitude was well within the range of the analog-to-digital converters, because linearity of propagation and detection is an important requirement for employing the synthetic backpropagation approach.

The transducer's two-way impulse response distorts the waveform of the pulse-echo data in comparison to the detected PA data. To match the waveforms of the synthetically generated and the real echo signals – and thus enable accurate subtraction – S and S^* were convolved with a matched pair of finite impulse response (FIR) filters, one for each type of signal. These filters were calibrated prior to the experiments in a simple setup with a plane steel reflector. An isotropic transmit and receive characteristic was assumed to be able to restrict filtering to the time dimension. The calibration measurements demonstrated that this approximation was roughly valid up to $\pm 20^\circ$ transmit/receive angle, which was sufficient for synthetic backpropagation in the proposed experiments. Waveform matching over a larger angle range requires plane-wave decomposition of detected signals for different receive directions, which would significantly increase the numerical burden.

The resulting synthetic data (PAFUSion data) was then transferred into the third buffer frame that was defined within the dummy PA acquisition. After that, PA image reconstruction was performed both on the second data frame (real PA image) and on the third data frame (PAFUSion image) using the Verasonics proprietary pixel-based reconstruction algorithm. In addition, the intensity of the PAFUSion image was scaled to match the PA image intensity. The identified reflection artifacts (PAFUSion image) were then subtracted from the PA image to obtain the corrected PA image. The corrected PA image was displayed along with the PA and PAFUSion image. The subtraction was performed on the reconstructed RF data prior to envelope detection, but the images were finally displayed as linear square envelope. In addition to the PA images, a synthetic aperture US image was reconstructed from the first frame data. For presentation in this paper, all the final results were additionally reconstructed offline from saved raw data by using frequency domain reconstruction algorithms [32].

The whole procedure can in principle be performed in real-time, limited only by the laser pulse rate (10 Hz). The signal acquisition speed for the element-wise pulse-echo data was similar to a conventional line-by-line scan. Two acquisitions (each on 64 elements) for the full probe aperture per transmitting element, times 128 for all transmitting elements, resulted in a total number of 256 acquisitions. With a 40 μ s round-trip time for 30 mm imaging depth, the minimum acquisition time for a full data set was roughly 10 ms, and a sampling rate of 20 MHz resulted in a data size of 12.8 Msamples and thus an estimated data transfer time of roughly 4 ms, considering the system's 14 bit sample size (roughly 2 Bytes) and transfer rate (6.6 Gbyte/s). Using the Verasonics proprietary pixel-based algorithm, reconstruction of the three images (US, PA, PAFUSion) required negligible time. The speed bottleneck in the current implementation of the technique was the synthetic backpropagation that was coded in Matlab, limiting the frame rate to one image every three seconds. Speed may be significantly increased and made real-time when using parallel processing, but this was not yet implemented in the present study. The quasi-real-time display was still helpful because it provided a visual feedback for aligning the imaging plane for optimum artifact reduction.

3.3 Phantom experiment

Figure 3 shows the schematic of the phantom and the setup used for the validation of synthetic backpropagation PAFUSion. The phantom consisted of one optical absorber (brown nylon thread, 0.28 mm diameter) positioned above an acoustic reflector (Delrin rod, 1.9 mm diameter). Both the optical absorber and acoustic reflector were placed inside a container filled with water, in such a way that they were perpendicular to the imaging plane of the US transducer that was immersed in the water. This phantom was used to study a comparatively simple scenario. No optical scattering agent was added to the water, to maximize the amplitude of the PA transient (and thereby of the PA reflection). In this experiment, the time T was selected in such a way that the PA signal from the thread and the delrin rod was backpropagated.

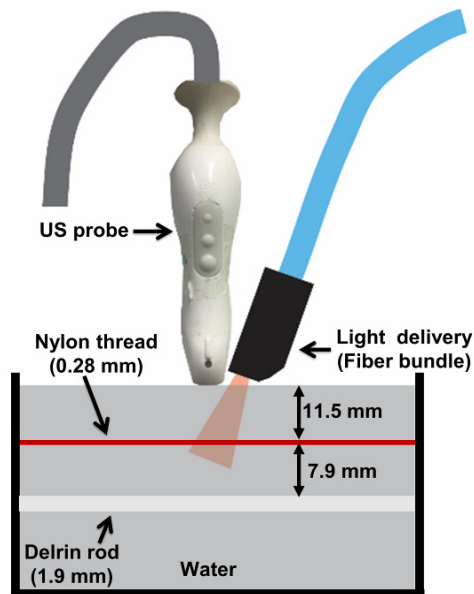


Fig. 3. Scheme of the phantom and experimental setup.

3.4 *In vivo* measurements on human forearm

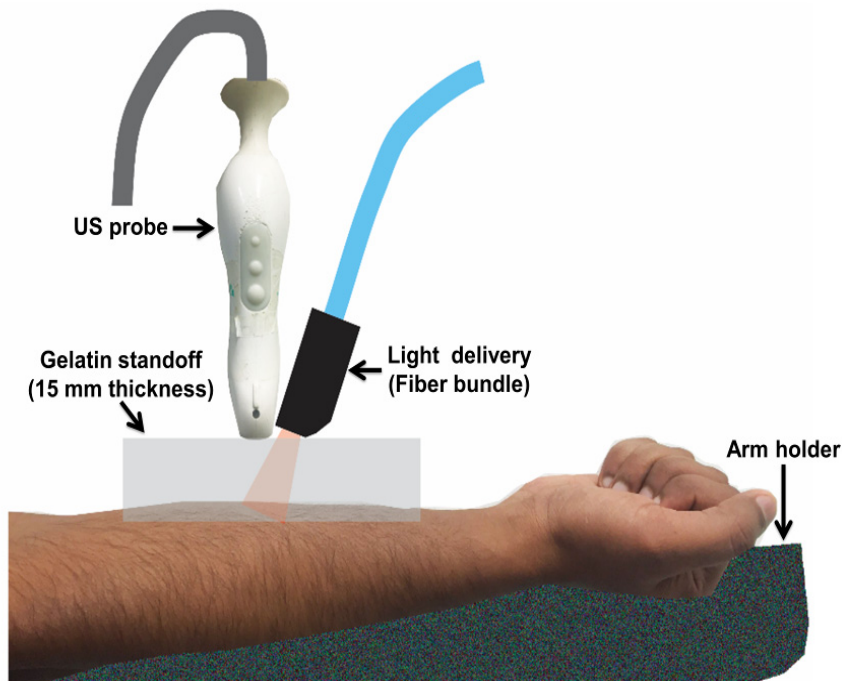


Fig. 4. Epi-mode PA/US setup used for the *in vivo* measurements.

The ability of PAFUSion to identify and eliminate reflection artifacts *in vivo* was investigated by measurements on a volunteer's right forearm. Considering the large number of optical absorbers (melanin, veins, arteries etc.) and acoustic reflectors (skin, muscle layers, fascia) in this area, one can expect a complex variety of reflection artifacts. To facilitate optical irradiation at the intersection of the skin and the imaging plane below the transducer aperture, we designed a gelatin stand-off pad (Fig. 4) that provided acoustic coupling over a distance of 15 mm in-between the forearm and the US probe. To minimize tissue motion in-between successive frames at the rather low frame rate while aligning the probe, the forearm was immobilized inside an arm holder as shown in Fig. 4. The US probe was aligned with the imaging plane perpendicular to the forearm and rigidly mounted along with the optical fiber bundle using a mechanical stage. Measurements were done at two different locations on the forearm, where reflection artifacts were well visible in PA images. The quasi real-time display of PA images provided feedback to aid selection of locations for measurements. In all *in vivo* measurements, T (time until which only real PA signals were expected) was selected in such a way that the PA signal from only the skin and the superficial blood vessels until 2 mm depth were synthetically backpropagated for PAFUSion.

3.5 Quantitative analysis of reflection-artifact-reduction

The efficiency of PAFUSion in reducing reflection artifacts was quantitatively assessed by offline processing. For this purpose, the pixel intensities of selected regions of interest (ROI) in the image were compared, before and after correction of PA images using PAFUSion. Regions of interest were selected based on the brightness of the features in the uncorrected PA image. All features with image intensities above a certain threshold were considered for the comparison. Few of them are indicated and discussed in the Results section. The pixel intensity of a ROI was calculated as the average intensity of 9 pixels (3 by 3) centred around the maximum intensity value in the area. For comparison, pixel intensities of the same

selected regions were determined in the uncorrected (PA_i) and in the corrected PA image ($CorrPA_i$). The ratio of PA_i and $CorrPA_i$ (Intensity reduction ratio = $PA_i / CorrPA_i$) was calculated and expressed in dB to highlight the potential of PAFUSion in reducing reflection artifacts.

4. Results

In all images, lateral and axial coordinates are represented by x and z respectively. The square envelopes of the images (PA, US, PAFUSion and corrected PA) are displayed in linear scale.

4.1 Phantom experiment

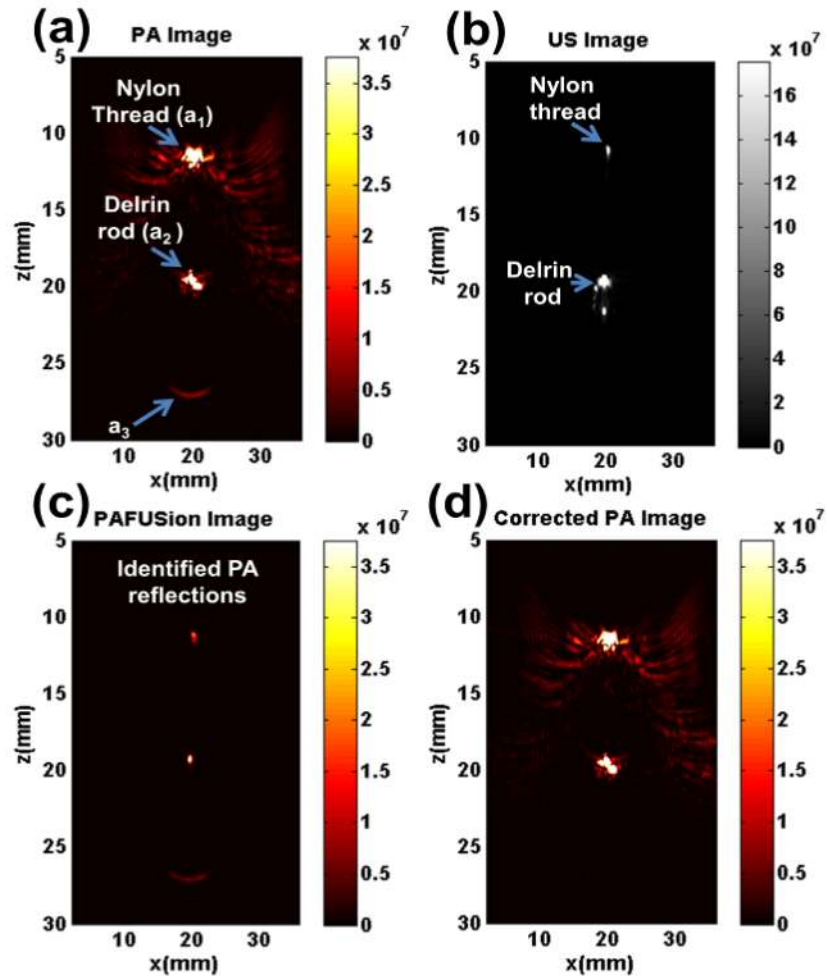


Fig. 5. Phantom experiment a) photoacoustic image, b) ultrasound image, c) PAFUSion image with identified reflection artifacts, d) corrected photoacoustic image.

Figure 3 shows a schematic of the phantom and the orientation of US probe in the experimental setup. This phantom contained one optical absorber (nylon thread) and an acoustic reflector (Delrin rod). Both the nylon thread and the Delrin rod are visible in the US image (Fig. 5(b)). Figure 5(a) shows the reconstructed PA image in which the nylon thread (marked as a_1 at $x = 20$ mm, $z = 11.5$ mm) and the Delrin rod (marked as a_2 at $x = 20$ mm, $z = 19.5$ mm) are visible. The wing-like artifacts near the nylon thread are grating lobes, caused by the rather large element pitch (0.298 mm) in comparison to the acoustic wavelength at the

center frequency of the transducer. They are more apparent in the PA image than in the US image owing to the different color map. Visibility of the Delrin rod in the PA image can be explained by optical absorption on its surface. In an ideal case, only the optically absorbing structures are expected to show up in the reconstructed PA image. However, a further feature is visible in the PA image at a depth around $z = 27$ mm (marked as a_3).

The PAFUSion image (Fig. 5(c)) evidently revealed that this feature is a reflection artifact, since shape and spatial details of the reflection generated by PAFUSion matches with the real PA feature. It is worth noticing that the PAFUSion image also suggests that reflection artifacts were present at the locations of the nylon thread and Delrin rod. Even though such reflection artifacts would not be distinguishable from the nylon thread/Delrin rod in the PA image, they may actually represent reality: Part of the PA transient that is generated at the thread/Delrin rod surface may be caused by heating of the adjacent water via heat conduction from the surfaces of the thread/Delrin rod. This part would then echo back from the nylon thread/Delrin rod itself, producing reflection artifacts at the location of generation of the PA transients. More likely, however, these artifacts may simply be the result of reflections of the backpropagated wavefield at the absorber surface, immediately before it converges at $t^* = 0$ to inside the absorber where the original PA transient was generated. Because these reflections occur before the hypothetical time zero, they do not correspond to real PA reflections but are an artifact of the backpropagation technique. In agreement with assumptions (i) and (ii), such echoes are not significant compared to the amplitude of the actual PA signal and thus could be omitted from the theoretical derivation. They are, however, noticeable when looking at the PAFUSion image alone. Similarly, echoes can already be generated when the backpropagated wavefield interacts with more superficial structures. The amount of such artifacts will therefore depend on the choice of T . The longer the backpropagated signal, the more false echoes can occur before $t^* = 0$ is reached.

Figure 5(d) shows the corrected PA image obtained by subtracting the PAFUSion-identified reflection artifacts from the real PA image. It is evident that the reflection artifacts are strongly reduced by using PAFUSion. The pixel intensities of three regions marked in the PA image as a_1 , a_2 and a_3 were compared with the same regions in the corrected PA image. The reflection artifact (a_3) intensity was found to be reduced by 12 dB. On the other hand, the intensities of the features a_1 and a_2 were reduced by only 0.005 dB and 0.35 dB respectively. These features can therefore correctly be assumed to be real PA sources. The slight reduction in PA signal of a_1 and a_2 resulted from the reflection artifacts that were identified (potentially wrongly) at the respective same locations. It is important to mention that this signal reduction – whether caused by true echoes or just by an artifact of the backpropagation – would always be proportional to the real signal. It will therefore not affect the relative amplitude of the signal, e.g. when scanning the tissue with multiple optical wavelengths for spectral PA imaging.

4.2 *In vivo* measurements on human forearm

Figure 6(a) shows one PA image out of the volunteer study (*in vivo* measurement 1). The orientation of the US probe and the forearm is indicated in Fig. 4. Figure 6(e) shows the same PA image, but with most of the various distinct features marked for reference. The skin signal (a_9) caused by the melanin is evident as a bright line at $z = 15$ mm. Three bright features (a_{10} , a_{11} , and a_{12}) are visible just underneath the skin signal, which may be three superficial blood vessels. Apart from these, the PA image contains plenty of diffuse features (a_1 to a_8) just below the skin and deeper inside the tissue. Figure 6(b) shows the synthetic aperture US image that contains many echogenic structures. The skin surface is visible as a specular reflection at $z = 15$ mm. Acoustic reflections from tissue structures inside the subcutaneous fat layer are visible as dotted echogenic features below the skin layer. The extended lines deep in the image at $z = 18$ mm to 20 mm are the epimysia between different muscles.

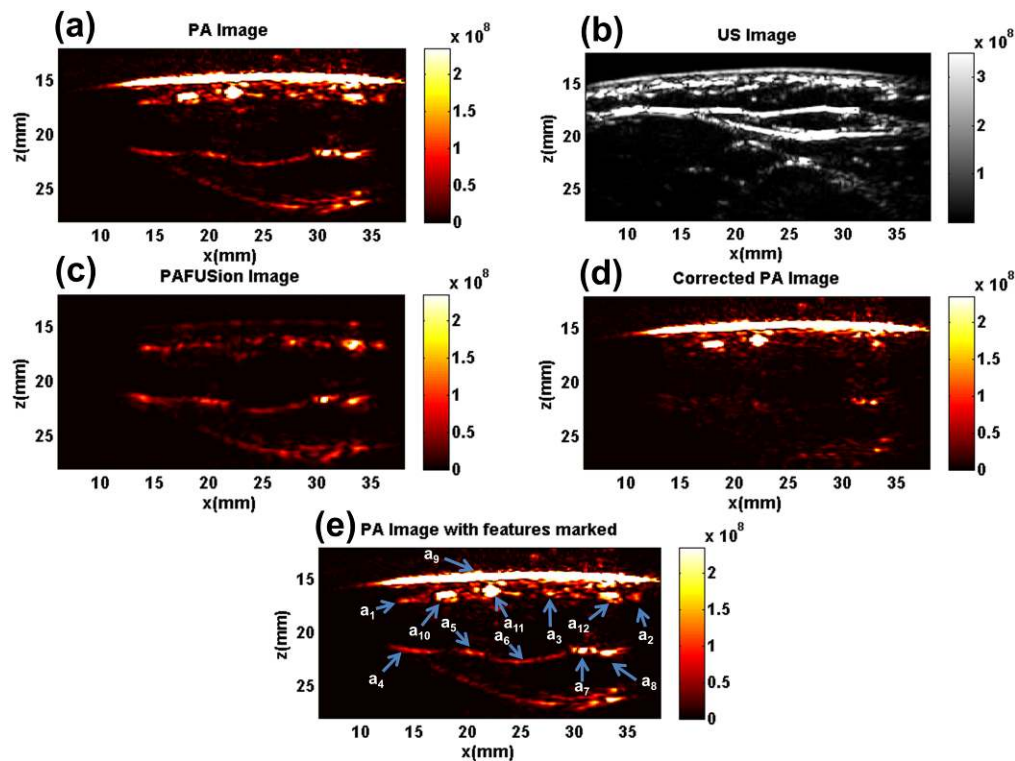


Fig. 6. *In vivo* measurement 1 a) photoacoustic image, b) ultrasound image, c) PAFUSion image with identified reflection artifacts, d) corrected photoacoustic image after subtraction of reflection artifacts, e) photoacoustic image with features marked for reference. The initial photoacoustic image followed by the corrected photoacoustic image after subtraction of the PAFUSion image is shown in [Visualization 1](#).

Figure 6(c) shows the PAFUSion image that shows only the simulated reflection artifacts. Our method demonstrates that the majority of the features in the PA image correlate with the simulated reflections. Except for a_9 , a_{10} , and a_{11} , all other features in the PA image (a_1 to a_8) are thus identified as reflection artifacts by the PAFUSion image. Similar to the phantom results, a reflection artifact was identified at the depth of the melanin layer itself (line like feature at around $z = 15$ mm). This may again correspond to a real reflection, as skin is optically absorbing as well as acoustically reflecting, or it may simply be an artifact of the technique in analogy to what was hypothesized in the phantom experiment. The amplitude of such reflections is significantly smaller than the amplitude of the PA signal and may be neglected under many circumstances. If not negligible, it is proportional to the PA signal. Therefore, the relative variation of the PA amplitude with wavelength will be unaltered in the corrected PA image, an important prerequisite for e.g. oxygen saturation determination. Figure 6(d) shows the corrected PA image obtained after subtracting the PAFUSion image from the PA image. All the identified reflection artifacts are strongly reduced in the corrected PA image. The remaining features in the corrected PA image are a_9 , a_{10} , a_{11} . The feature a_{12} is of special interest: In PAFUSion image, a much brighter signal is visible exactly at the same location as a_{12} , but this feature persists in the corrected PA image. This feature might therefore well be a blood vessel that was initially mixed with a reflection artifact from which it was recovered. Two features visible at depth in the corrected PA image ($x = 32$ mm, $z = 22$ mm and $x = 33$ mm, $z = 26$ mm) may be deeper blood vessels, which were recovered from surrounding reflection artifacts, but could also be the result of inaccurate image subtraction. It is especially worth mentioning that PAFUSion identified most of the PA features located directly below the skin as reflections that would normally be interpreted as real PA signals.

Depending on the clinical applications, it may be of paramount importance to get rid of these artifacts for accurate image interpretation.

The ratio of PA image intensity before and after correction was calculated for all the regions marked in the PA image. These values are summarized in dB scale in Table 1 to quantitatively validate the efficiency of PAFUSion in reducing reflection artifacts.

Table 1. Intensity reduction ratio of all the marked regions in the PA image for *in vivo* measurement 1.

Region of interest	a ₁	a ₂	a ₃	a ₄	a ₅	a ₆	a ₇	a ₈	a ₉	a ₁₀	a ₁₁	a ₁₂
Intensity reduction ratio (dB)	8.5	14	18	9	13	11	22	15	0.6	0.4	0.5	7

Table 1 demonstrates that the intensities of features a₁ to a₈ (reflection artifacts) are significantly reduced in the corrected PA image, with an average reduction of around 13 dB. The intensities of features a₉, a₁₀, and a₁₁, were reduced by around 0.5 dB which is significantly less than what was measured for a₁ to a₈, substantiating the hypothesis that these were real PA sources. The intensity of a₁₂, which is still well visible in the corrected image, is reduced by 7 dB which is in the middle dB range, supporting the assumption that this was a real PA source which was initially mixed with a reflection artifact.

Figure 7(a) shows the PA image from a slightly different location on the same forearm (*in vivo* measurement 2). Figure 7(e) shows the same PA image, but with several selected bright features (a₁ – a₉) marked for reference. The skin signal is visible as a bright arc at a depth of around 16.5 mm (a₅). The double layered feature just below the skin (a₇) may be a superficial blood vessel. Several other bright features are visible in the PA image. Among them are: 1) A blob-like structure (a₆) below the skin and in proximity to a₇; 2) a prominent double layered feature a₉ and 3) the extended line-like structure (a₈) close to a₉. Several other features are visible in the PA image out of which a few are marked in Fig. 7(e) (a₁ – a₄). In such a scenario, it is difficult to differentiate between real PA features and reflection artifacts. Similar to the *in vivo* measurement 1, Fig. 7(b) shows the synthetic aperture US image in which different echogenic structures are visible that may lead to PA reflection artifacts.

The PAFUSion image (Fig. 7(c)) shows the identified reflection artifacts. Again, in this measurement, our method shows exceptional potential in exposing that more than 60% of the bright features in the PA image of the forearm were reflection artifacts. Except for some structures (a₅ to a₉), all other features (a₁ to a₄) are identified as reflection artifacts, including other features that were not marked in the PA image (Fig. 7(e)). All the identified artifacts are in close proximity to real PA features, confounding the image interpretation. A reflection artifact is identified at the depth of the skin-melanin layer (line like feature at around 16.5 mm depth), as in the previous results. Owing to the optical and acoustic contrast of the skin, this may be a real reflection artifact or an artifact of the technique as hypothesised in previous results. Figure 7(d) shows the corrected PA image obtained by subtracting identified reflections (PAFUSion image) from the PA image. All the identified reflection artifacts are significantly reduced in the corrected PA image. The bright features left in the corrected PA image are a₅ to a₉. In this measurement also, PAFUSion identified several puzzling reflection artifacts below the skin surface and in the location where small blood vessels are expected. One of the examples is the bright feature a₂ in the PA image (Fig. 7(e)). The intensity of this feature is strongly reduced in the corrected PA image (Fig. 7(d)), which aided in a better interpretation of the double-layered structure a₇, which might well be a blood vessel. Another example is the feature a₄ marked in the PA image (Fig. 7(e)). This structure along with another less bright feature below it could be misinterpreted as a big blood vessel. After applying PAFUSion, it is clear that this feature is a reflection artifact as it is substantially reduced in the corrected PA image (Fig. 7(d)). Another important feature to be discussed is a₈, which very well might be misinterpreted as a reflection artifact based on its extended shape. After applying our method, it is clear that a₈ is a real PA feature (possibly from a small vessel running along the muscle perimysium).

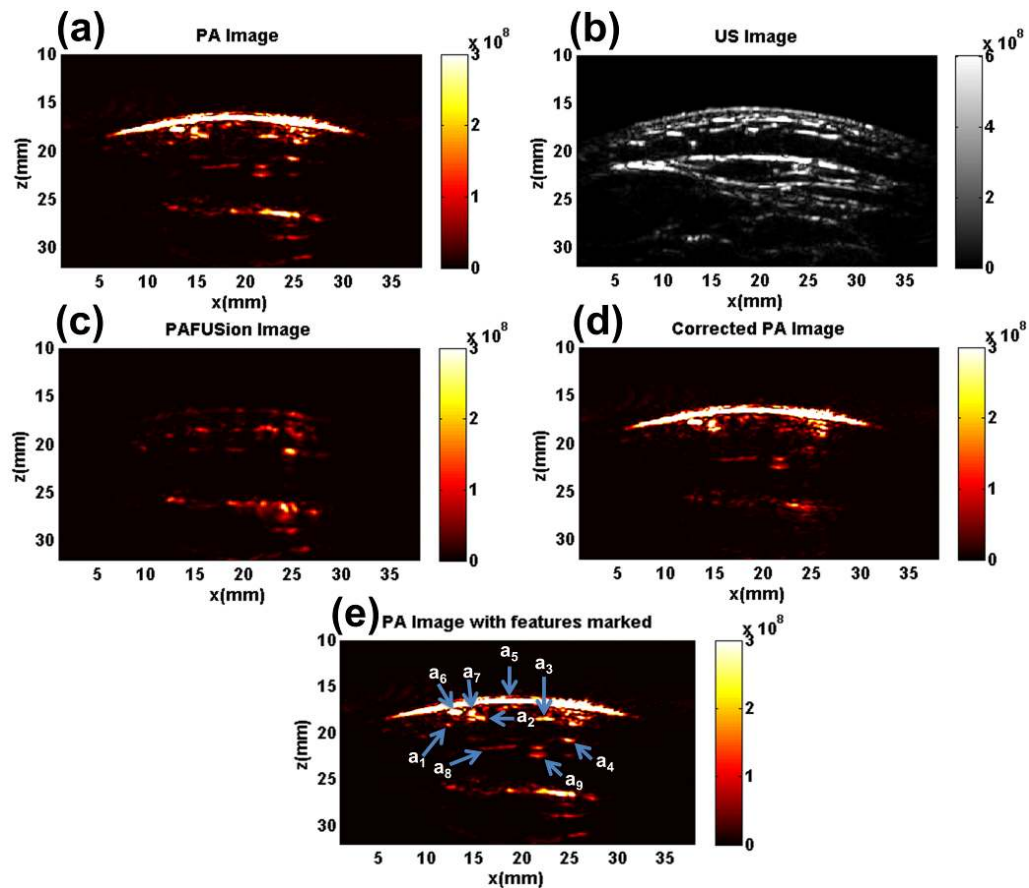


Fig. 7. *In vivo* measurement 2 a) photoacoustic image, b) ultrasound image, c) PAFUSion image with identified reflection artifacts, d) corrected photoacoustic image, e) photoacoustic image with features marked for reference. The initial photoacoustic image followed by the corrected photoacoustic image after subtraction of the PAFUSion image is shown in Visualization 2.

All the reflection artifacts were accurately identified in the PAFUSion image (Fig. 7(c)), maintaining the shape and the spatial details. Intensity reduction ratios were calculated for all the marked regions in the PA image. Table 2 summarizes these ratios for all the selected regions in the PA image for this measurement (*in vivo* measurement 2). It is clear from Table 2 that the intensity of features a_1 to a_4 (reflection artifacts) are significantly reduced in the corrected PA image, with an average reduction of around 13 dB. For real PA features a_5 to a_9 , the intensity were just reduced by less than 0.3 dB which is significantly less compared to the intensity reduction of artifacts.

Table 2. Intensity reduction ratio of all the marked regions in the PA image for *in vivo* measurement 2.

Region of interest	a_1	a_2	a_3	a_4	a_5	a_6	a_7	a_8	a_9
Intensity reduction ratio (dB)	18	9	9.5	13	0.4	0.2	0.3	0.1	0.1

5. Discussion

The phantom as well as the *in vivo* results demonstrated that PAFUSion using synthetic backpropagation is capable of identifying and strongly reducing reflection artifacts in epi-

mode PA imaging. Using this technique, the reflection artifact intensity was reduced by around 13 dB on average in both phantom and *in vivo* measurements. The aim of this study was to give proof-of-principle of *in vivo* artifact reduction using synthetic backpropagation. However, PAFUSion might also be suitable for a quantitative investigation of reflection artifact occurrence (e.g. relative intensity compared to direct PA signals, as function of depth). First conclusions can be drawn from the presented *in vivo* results. In measurement 1, the features a_1 to a_6 that were identified as reflection artifacts had intensity levels that were between 14 dB and 17 dB lower than the intensity of the melanin signal from which these reflections originated. Features a_7 and a_8 were also identified as reflections, but only 9 dB below the melanin signal. Similar to measurement 1, the reflection artifacts a_1 to a_4 in measurement 2 were between 10 dB and 13 dB below the melanin signal level. In comparison, the blood vessel signal (a_9) was 13 dB below the melanin signal level. This demonstrates that the intensity of reflection artifacts gets comparable to true PA signal intensity already at a depth of only 5 mm below the skin surface.

For the first time, we demonstrate identification and strong reduction of a large number of reflection artifacts just beneath the skin and in proximity to superficial vasculature. In a conventional image, these artifacts may well be misinterpreted as small blood vessels, thus demonstrating the importance of PAFUSion in identifying and reducing them. Previously reported PA clutter reduction techniques are good at reducing artifacts in deeper tissue for improving imaging depth [24, 26], but are not suited for improving contrast in shallow tissue. Removal of reflection artifacts in the region directly below the skin by using PAFUSion can help to avoid false interpretation of these features as blood vessels, inflammations, and/or a cancerous tissue. In a clinical scenario, the PAFUSion image itself will already be relevant for identifying true features in the PA image. However, reduction of reflection artifacts in the PA image via subtracting the PAFUSion has the added benefit of uncovering true PA features that are else hidden by reflection artifacts.

A main advantage of PAFUSion is that it can be implemented in any dual-mode PA/US system that provides sufficient acquisition control. Compared to LOVIT [24], it does not require US powers close to the safety limit. Compared to DCA [26], it can be used without extensive training. It is not restricted to a certain frequency band, whereas LOVIT and DCA work efficiently for the upper frequency band where a significant displacement can be achieved in comparison to the acoustic wavelength. The synthetic implementation of PA backpropagation based on reference pulse-echo data is completely software based, which makes implementation of this method in a clinical system straightforward. In this work, the backpropagation algorithm was implemented in Matlab. This was the bottleneck for processing speed and resulted in a rather slow overall framerate of around one image per three seconds. However, the display rate will be significantly improved by implementing this method on GPU (Graphical processing units). In the proposed version of PAFUSion, the reference pulse-echo data was based on single element transmissions. A different option is to use plane-wave transmissions with multiple angles. In plane-wave transmissions, the array elements are excited in a sequence. For large angles, this has the disadvantage of a long dead time during which element cross-talk can occur from transmitting elements resulting in cross-talk artifacts that obscure echoes from close to the transducer. However, this may not have a significant influence, if a gel spacer between the probe and the skin adds a sufficient delay to the arrival of first PA signals. An advantage of a plane-wave transmission approach is that it is conceptually more close to a frequency-domain formulation (with decomposition into plane-wave components) than the element-wise approach. Schwab *et al* [29] utilized a comparable model-based approach in which multi-angled plane-wave US transmissions were used to imitate the reflected PA waves. They derived a mathematical relation in frequency domain that links the plane-wave US measurements and a reflection-artifact-free PA measurement to the actual PA measurement. This relation is inverted in order to attain a reflection-artifact-free PA measurement. Preliminary simulation and phantom results were demonstrated. Such an inverse-problem approach may help avoid false reflections in the PAFUSion image, and require less US acquisitions by making use of data redundancies.

At this point, we would like to draw the attention to a limitation of the proposed technique: PA backpropagation is limited to the part of the wavefield that can be simulated by the transducer. In case of a linear array probe with limited aperture and limited transmit angle range, only transients that propagate parallel to the imaging plane and within that angle range and aperture can be reproduced by US transmission. As already predicted in the theory section, the experimental results demonstrate that this limitation is not crucial. The most important PA source – the melanin layer – could easily be aligned perpendicular to the imaging plane, aided by the quasi real-time feedback of the image display. In addition, the PA transient generated by the melanin layer contains only directional components running axially within the angular transmit aperture of the probe. The laterally propagating transients generated by the superficial blood vessels, on the other hand, do not seem to have produced significant reflection artifacts. PAFUSion is specifically designed for reducing the echoes of the PA transients that are generated in the measurement plane. Only such echoes can be mimicked via backpropagation from the probe aperture, whereas the out-of-plane echoes, particularly strong when irradiating outside the probe cannot be reduced. In-plane irradiation is required for maximizing SNR of direct PA signals when using integrated systems with low diode laser pulse energies, but at the same time it limits contrast owing to the resulting echoes. PAFUSion is ideally suited for such systems, for reducing the superficial echoes within the limited imaging depth that results from the low SNR.

Another important point to consider is the role of US attenuation in the applicability of the technique. When backpropagating the PA signal to the origin, it has undergone propagation through the tissue twice, resulting in additional attenuation compared to the real PA transients that generate the reflection artifacts. Therefore, it is expected that the synthetically mimicked echoes do not perfectly match the real ones. This apparently did not play much of a role in our experiments, owing to the shallow imaging depth. For applications requiring larger imaging depth, this problem is expected to become prominent. We foresee to solve this by a depth-dependent impulse response matching, based on an assumed attenuation map of the tissue.

All clinical applications of epi-mode PA imaging could benefit from the efficient reflection artifact correction achieved using our novel method. One of the important sources of PA reflection artifacts is the skin melanin layer. Thus, PAFUSion will help to avoid the exclusion of dark skinned patients from PA clinical measurements/clinical trials. The impact of PAFUSion will also be high for imaging structures such as finger joints or wrists where multiple small blood vessels and highly reflecting tendons and bones are present in a dense space. Furthermore, reflections of high PA transients generated at the tip of the optical fiber is a well-known problem in PA guidance of minimally invasive procedures [33–35]. These reflection artifacts can be potentially identified and reduced using the proposed technique.

The present study focused on reflection artifact reduction in epi-mode PA imaging using handheld probes. Reflection artifacts generated by PA transients from the skin surface are most disturbing in epi-PA imaging because they overlap in time with the weak PA signals from inside the tissue where the fluence is comparably low. In comparison, tomographic systems with curved arrays in two or three dimensions typically use a transmission- or orthogonal-mode irradiation geometry, where a better distinction may be possible because the fluence inside the tissue is relatively higher. However, strongly reflecting structures such as air-filled cavities or bones can lead to prominent reflections in PA tomography of small animals. It has been shown that significant artifact reduction is possible by using a weighted back-projection approach, where image reconstruction is selectively based on PA signals that are least disturbed by reflectors [30]. We hypothesize that PAFUSion will even be helpful in such systems because it allows artifact reduction without data reduction, potentially providing improved spatial resolution of real PA sources.

6. Conclusions

In summary, PAFUSion can identify and strongly reduce in-plane reflection artifacts, and thus envisions potential in improving PA imaging of acoustically inhomogeneous tissue. In both phantom and *in vivo* measurements, the intensity of reflection artifacts was on average

reduced by around 13 dB, which is certainly a promising result. For the first time, we demonstrated the relevance of identifying and reducing superficial PA reflection artifacts to improve image interpretation. PAFUSion will thus be a useful addition to any epi-mode PA/US system.

Acknowledgments

Research leading to these results was funded by the European Community's Seventh Framework Programme (FP7/2007-2013) under grant agreement n° 318067. Authors acknowledge Dr. Altaf Hussain for his insightful discussions and help.